Section 1
PROGRESS IN LASER FUSION

1.A Observations of Enhanced Thomson Scattering

The scattered-light spectrum from a laser-produced plasma includes several frequently observed features, such as the even and odd half-harmonics of the laser frequency. These features are fairly well understood and can be explained in terms of parametric instabilities or resonance absorption. We have, however, found three large spectral features that are not easily explained in terms of parametric instabilities. One lies between the laser frequency (ω_0) and its half-harmonic ($\omega_0/2$) and will be referred to here as the down-scattered band. The other two are up-scattered bands near $3\omega_0/2$, one above this value and one below.

These features can be explained by an enhanced Thomson scattering (ETS) model.[1-3] Briefly, these enhanced scattering bands arise from Thomson scattering of the pump laser on density variations that have been enhanced by the presence of pulses of fast electrons.

This model has three parameters, which determine the position of a scattering band: the background ("cold") electron temperature; the central directed velocity of the fast-electron pulse; and the relative numbers of fast electrons in the pulse. The directed velocity can be inferred from a time-integrated measurement of a hot-electron "temperature." Experiments were conducted to independently measure the location of the scattering bands and the hot- and cold-electron temperatures.

Previous experiments[4,5] concentrated on the down-scattering feature, on the supposition that it is the signature for the convective stimulated Raman scattering (SRS) instability. A recent paper[6] observed both up- and down-scattered bands and explained the presence of the up-scattered band as due to anti-Stokes mixing.

Theory

The SRS instability occurs as a result of the coupling of a scattered electromagnetic (EM) wave, with a fluctuation in a plasma wave through the presence of an oscillating EM pump wave. An initial-density perturbation (noise) produces a transverse current due to the oscillatory pump wave, which in turn produces a reflected EM wave. The ponderomotive force of the interacting incident and reflected EM waves enhances the initial-density perturbations.[7] This feedback mechanism will amplify any initial noise (plasma-wave amplitude) exponentially until the instability saturates by convection or by some nonlinear process. To initiate this cycle, the pump wave must be strong enough to overcome any losses in this system, including convection and damping of the waves. Therefore, a threshold pump power (i.e., threshold laser intensity) will exist for SRS.

Even below the threshold for the SRS instability, there will still be low-level scattering of EM light by interaction of the pump wave with collective thermal fluctuations in the plasma. This scattered EM light is what is called the "electron line feature" of classical Thomson scattering. As long as the plasma waves are at thermal levels, the fractional energy scattered this way is quite small. If for some reason the electron distribution deviates significantly from Maxwellian, however, considerable enhancement of some of the plasma-wave levels may exist. In such a case, enhancement of the Thomson scattering may occur and could easily be mistaken for a signature of SRS.

Even when the SRS threshold is exceeded, the exponential growth proceeds from the initial noise level. Those plasma densities at which enhanced plasma-wave levels exist contribute most efficiently to the SRS signal; thus, this enhanced "seed" may still determine the frequency spectrum of the observable Raman scattering.

For a given plasma density, the scattered light and plasma waves must satisfy the following energy and momentum matching conditions for the SRS instability to occur:

$$\begin{aligned} \omega_0 &= \omega_s + \omega_p \\ k_0 &= k_s + k_p \quad , \end{aligned} \tag{1}$$

where ω_0 (k_0), ω_s (k_s), and ω_p (k_p) are the frequencies (wave vectors) of the laser, scattered-light wave, and plasma wave, respectively. In addition, the scattered EM and plasma waves must satisfy the relevant dispersion relations:

$$\begin{aligned} \omega_0^2 &= \omega_{pe}^2 + c^2 k_0^2 \\ \omega_s^2 &= \omega_{pe}^2 + c^2 k_s^2 \\ \omega_p^2 &= \omega_{pe}^2 + 3 v_T^2 k_p^2 \quad , \end{aligned} \tag{2}$$

where ω_{pe} is the plasma frequency, c is the speed of light, and v_T is the electron thermal velocity. Taken together, Eqs. (1) and (2) imply that the frequency of the scattered light is proportional to the plasma density at its origin and that the scattered SRS EM wave may occur only in the frequency interval[8] $\omega_0/2 < \omega_s < \omega_0$. The threshold for convective SRS (SRS-C) in an inhomogeneous plasma is given by[9]

$$\left(\frac{v_o}{c}\right)^2 k_0 L > 1 \ , \tag{3}$$

where v_o is the electron oscillatory velocity, k_0 is the laser wave number inside the plasma, and L is the plasma scale length. In practical units, the threshold condition on the incident intensity may also be written as

$$I_{\text{thres}} = \frac{4.4 \times 10^{17}}{L_\mu \lambda_\mu} \frac{\text{W}}{\text{cm}^2} \ , \tag{4}$$

with L_μ and λ_μ expressed in microns. In our experiments,[10] $\lambda_\mu = 0.527$ and $L_\mu \sim 80$, corresponding to an intensity threshold of 1×10^{16} W/cm^2.

Enhanced Thomson scattering, in contrast, has no threshold as such, but does require an electron distribution that is non-Maxwellian. The theory in Ref. 1 assumes that bursts of energetic electrons are produced at the quarter-critical density surface by the onset of parametric instabilities, such as absolute stimulated Raman scattering (SRS-A)[11] and two-plasmon decay (TPD).[12] At the critical surface, resonance absorption (RA), although not a parametric instability, can also produce energetic electrons.[13] These bursts move out into the plasma and can be reflected at sheaths. Locally, this produces a transient, "bump-on-tail" electron velocity distribution if the number of hot electrons exceeds some minimum value. Because of the subsequent isotropization and slowing of these fast electrons, any time-integrated measurement of their x rays can be interpreted in terms of an effective "hot"-electron temperature T_h. According to the theory in Ref. 1, this temperature is related to the initial directed velocity of the burst, v_d, by $mv_d^2 = 3K\ T_h$. We expect that the time-integrated x-ray spectrum of our plasma can be interpreted in terms of a cold-electron temperature T_c, corresponding to the background thermal electrons; plus a hot component T_h from RA (if present); and a "superhot" component T_{sh} from SRS-A and TPD. For the conditions in our experiments, the cold temperature is typically between 0.8 and 2 keV, the hot temperature is between 5 and 10 keV, and the superhot temperature can range between 15 and 60 keV. Most of the electrons are in the cold component.

If it is assumed that the fast-electron bursts move up and down along the direction of the density gradient, it is possible to calculate the resulting enhanced Thomson scattering. Computer calculations show that the enhanced scattering in an inhomogeneous plasma will occur in two bands: one, a down-scatter band between ω_0 and $\omega_0/2$; the other, an up-scatter band between $2\omega_0$ and ω_0. The two bands are not symmetrical about ω_0, nor need they have the same minimum

number of fast electrons (i.e., the same threshold) for the enhancement to occur.

If there are two distinct hot temperatures identified in an experiment, a second pair of enhanced bands is expected to be present. However, the minimum number of hot electrons required may vary considerably from band to band, and so not every band need be observed in any given experiment.

Of course, the spectral location and width of the bands are also functions of three variables: the angle of incidence of the laser relative to the density gradient, the angle of observation, and the average ionic charge. All these variables have been included in a numerical calculation. The result is usually insensitive to the value of T_c, and the central location of the band does not vary appreciably when the fraction of hot electrons is increased above some minimum value.

An example of a simulated spectrum for the conditions of this experiment, including refraction, is shown in Fig. 34.1, where the enhanced wavelength bands are shown as a function of f_h, the fraction of directed hot electrons in the pulse relative to the background density. This calculation assumed a tilted target at 45°, a laser wavelength of λ_o = 527 nm, an average ionic charge of Z = 3, a cold temperature of T_c = 1.5 keV, and a typical superhot temperature of 30 keV. There is as yet no reliable theory that will predict the number of hot electrons; hence, f_h is unknown. Fortunately, the central location of each band is insensitive to the value of f_h. As an example, if the superhot electron fraction f_{sh} is equal to 1%, Fig. 34.1 then predicts an up-scattered band between 286 and 350 nm and a down-scattered band between 777 and 920 nm. Note that this theory naturally predicts a gap between the long-wavelength limit of the down-scattered feature and the half-harmonic at 1054 nm. Also noteworthy is that the up-scattering feature extends well below the three-halves harmonic.

Figure 34.1 also shows the additions to the predicted spectrum if a third temperature, the hot component, is present. An additional pair of bands is added. As an example, for a hot temperature of 10 keV and a hot-electron fraction of 8%, there will be up-scattering between 360 and 400 nm, on the long-wavelength side of the three halves, and down-scattering between 690 and 760 nm. We would have observed a four-peaked spectrum if a large fraction of the electrons had been in the hot and superhot components.

There are several points in Fig. 34.1 that will be useful to note when interpreting experimental results. First, the down-scattering signals can be easily confused with the signal from SRS-C, since it also occurs between $\omega_o/2$ and ω_o. Furthermore, the short-wavelength cutoff is at about the same wavelength because its basic cause, Landau damping, is the same for both SRS-C and ETS. Various theories have been proposed to explain the long-wavelength gap near $\omega_o/2$ in SRS. These explanations include density steepening and suppression by ion waves, but none of these are quantitative as yet. Therefore, if only the down-

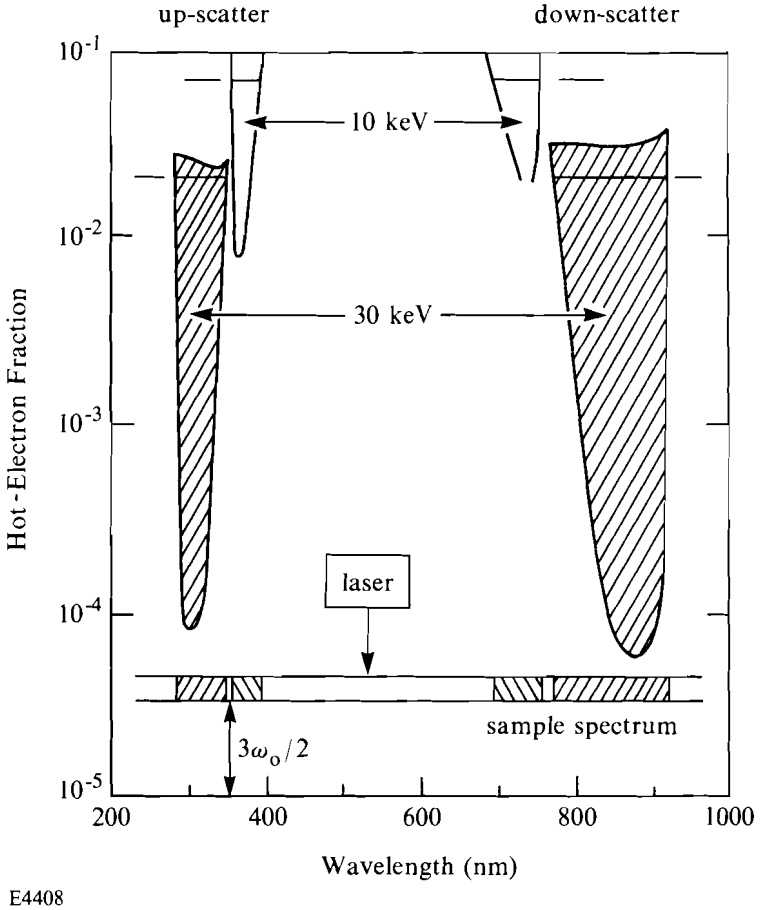

Fig. 34.1
Predicted enhanced Thomson scattering bands as observed in the direction normal to the target, assuming a three-component temperature distribution with T_c = 1.5, T_h = 10, and T_{sh} = 30 keV. The target is tilted at 45° and has Z = 3. The laser wavelength is 527 nm.

scattered signal is measured, SRS-C and ETS are difficult to distinguish. In addition, the superhot-electron fraction threshold for down-scattering is much lower than that for scattering caused by hot electrons. It is entirely possible that only the superhot down-scattering band will be observed. Finally, while the superhot-electron fraction threshold for down-scattering is lower than that for up-scattering, the reverse is true for the hot features. In fact, the hot up-scatter threshold is less than half that for the hot down-scatter threshold. It is therefore possible that there are enough hot electrons to produce the up-scattering band but not enough to produce the corresponding down-scattering band.

Experiments

A series of experiments using the glass development laser (GDL) system[14] at LLE was conducted to observe the anomalous scattering bands. GDL is a single-beam Nd:glass system that, for this series of experiments, delivered up to 200 J at 1.054 μm. Frequency doubling produced on-target energies of up to 60 J at 527 nm. The pulses were Gaussian in time and usually had a pulse width of approximately 600 ps after frequency conversion, although some experiments were done

with 1-ns pulses. The beam was focused onto 50-μm-thick Mylar targets by an $f/3.6$ lens. The x-ray spot size at 10% of the maximum intensity, as measured by an aluminum and beryllium-filtered pinhole camera, was 120 μm at best focus. This corresponds to a maximum average on-target intensity of 8×10^{14} W/cm^2.

Precautions were taken to limit the amount of blue (third-harmonic) and red (fundamental) energy on target. Residual 1.054-μm light intensity was reduced by the use of an IR absorber plate, dichroic mirrors, and by the chromatic shift of the focusing lens, resulting in $I_{1054\ \mathrm{nm}} = 10^{-9}\, I_{527\ \mathrm{nm}}$.

Scattered light was collected by two spherical aluminum mirrors each subtending a solid angle of 0.087 sr and focused onto the entrance slits of two, 0.25-m spectrometers. The first (UV) spectrometer, which incorporated a cross Czerny-Turner design with a 275-mm focal length and used a 600-groove/mm grating blazed at 300 nm, was usually tuned to observe the spectrum between 250 and 425 nm in order to view the up-scattered feature; the spectrum was recorded on Kodak 2495 film, with a resolution of better than 1 nm. The second (IR) spectrometer, which was used to view the down-scatter at wavelengths longer than 600 nm, was a quarter-meter Ebert monochromator equipped with a 170-groove/mm grating blazed at 500 nm. When used to view the time-integrated down-scatter, as in the first geometry [Fig. 34.2(a)], the signal was recorded on Kodak 4143 high-speed IR film. The spectral range was limited on the long-wavelength side to 925 nm by the falloff in film response. The short-wavelength side was limited to 570 nm by the use of sharp-cut, long-pass filters to reduce stray 527-nm light.

Three target/observation geometries were used. The first [Fig. 34.2(a)] had the laser normally incident onto the target and the mirrors placed at 135° from the forward direction. In this case, the two spectrometers were sampling the same observation angle. The second geometry [Fig. 34.2(b)] had the target tilted at 45°. The collection mirrors were at the same angles with respect to the laser so that the down-scattered spectrum was collected from the direction normal to the target and the up-scattered spectrum was observed along the target face (90° sidescatter). The third geometry [Fig. 34.2(c)] employed a similarly tilted target, but only one collection mirror was used, sampling along the target normal. The scattered light was directed onto the down-scatter spectrometer. A portion of this light was split off by an uncoated microscope slide that acted as a 4%-per-surface beamsplitter. Only the front surface reflectance was directed onto the up-scatter spectrometer. The use of an aluminized 10% beamsplitter in place of the uncoated glass reduced the down-scatter signal below detectable levels.

The IR spectra was also time resolved for all three geometries (Fig. 34.3). The output of the IR spectrometer was focused onto a streak camera slit by a pair of lenses: first, a cylindrical field lens with a 400-mm focal length used to collimate the spectrometer output, and second, a convex lens with a 43-mm focal length. The streak camera

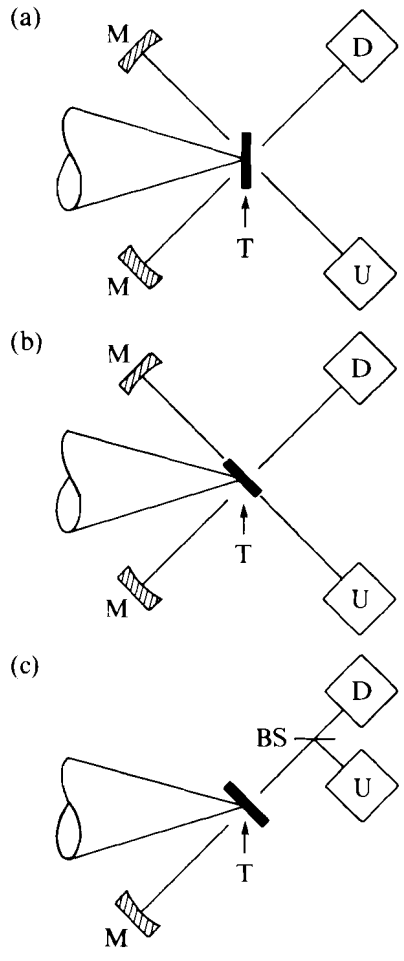

Fig. 34.2
Three detector/target geometries were used in the experiment. The scattered light is collected by two aluminium mirrors and focused onto the spectrometer slits with an effective f number of 13. In (a), both the up- and down-scattering signals are observed at 135° from the direction of laser propagation. In (b), the target was tilted at 45° to the laser with the observation angles unchanged. In (c), signals were sampled in the direction of the tilted target normal. The mirrors are labeled by *M*, the up-scattering (UV) spectrometer by *U*, the down-scattering (IR) spectrometer by *D*, the beamsplitter by *BS*, and the target by *T*.

and spectrometer slits were crossed to give both time and spectral resolution. The optics between the streak camera slit and the photocathode were corrected so that the effects of chromatic shifts were reduced.

An Imacon 675 streak camera equipped with an S-1 tube whose response peaked at 750 nm and fell off rapidly to either side, becoming ten times less sensitive at 1.05 μm, was used. The S-1 tube was very old and its sensitivity to 1-μm light has degraded to an even lower sensitivity. Streak data were taken at a sweep speed of 100 ps/mm. Due to the finite size of the photocathode, the spectral window was limited to 450 nm with a resolution of 10 nm.

The dispersion of the spectrometer/streak camera combination was determined by directing the output of two HeNe lasers, operating at wavelengths of 628 and 543.5 nm, onto the spectrometer slit. The grating was set so that the first-order red and second-order green and

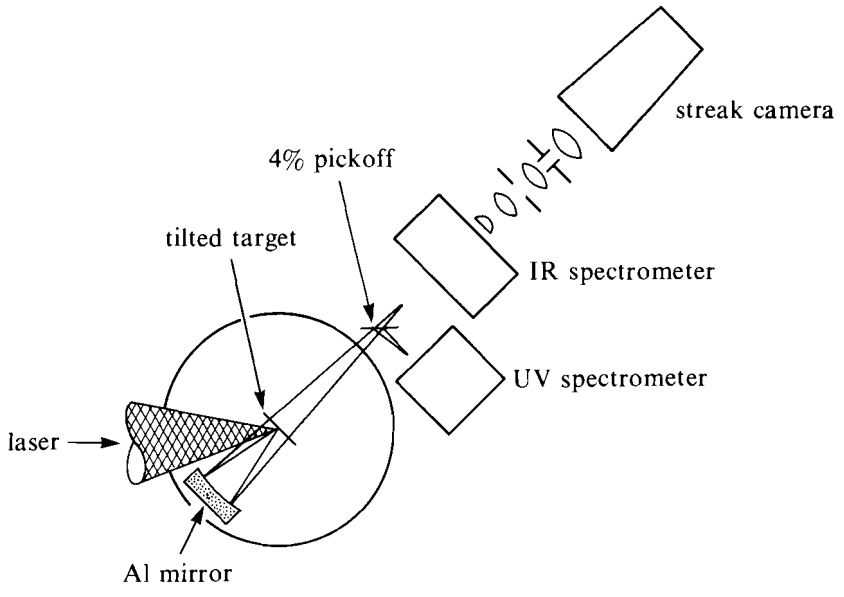

Fig. 34.3
Schematic layout for measuring the time-resolved down-scattering spectra. The optics between the streak camera slit and the photocathode were wavelength corrected to reduce chromatic distortion. The up-scattered signal was split off from the down-scattered by an uncoated glass slide.

red lines could be seen on the streak camera image intensifier phosphor when in focus mode. For an absolute wavelength fiducial, the IR absorber plate was removed from the incident laser beam, the lens was defocused, and low-energy ($<<$1-J) shots on gold targets, tilted at 22.5°, were taken to record the unconverted fundamental laser line. This also gave a temporal dispersion measurement. The data was recorded on Kodak Tri-X film, which was push processed to an equivalent ASA of at least 4,000.[15]

To determine the electron temperature, the x-ray continuum from the target was measured and a two- or three-Maxwellian electron distribution was fit to it.[16] The x-ray detectors consisted of nine PIN diodes and six scintillator-photomultiplier tube units filtered with various K-edge filters. In this experiment, the best results were obtained assuming a two-temperature model with cold and superhot temperature components. The former is characteristic of the dense plasma above n_c, while the latter is characteristic of nonlinear processes involving plasma waves at or below $n_c/4$. A third, or hot, component, which is characteristic of interaction phenomena near n_c (resonance absorption and/or the parametric decay instability) was not observed because its x-ray signal was too weak. We emphasize that this temperature measurement is independent of scattered light measurements.

Results

We first report on the time-integrated spectra obtained using the geometry of Fig. 34.2(a). The observation angles were both 135°, so our observations are affected by refraction, especially in the down-scatter measurement. Figure 34.4 shows three typical spectra. As the

incident intensity is increased (which would correspond to raising the superhot electron temperature), the long-wavelength shoulder increases in intensity and its long-wavelength cutoff increases. The long-wavelength sensitivity of our data is limited because of the extremely sharp cutoff, 925 nm, of the Kodak 4143 film used.

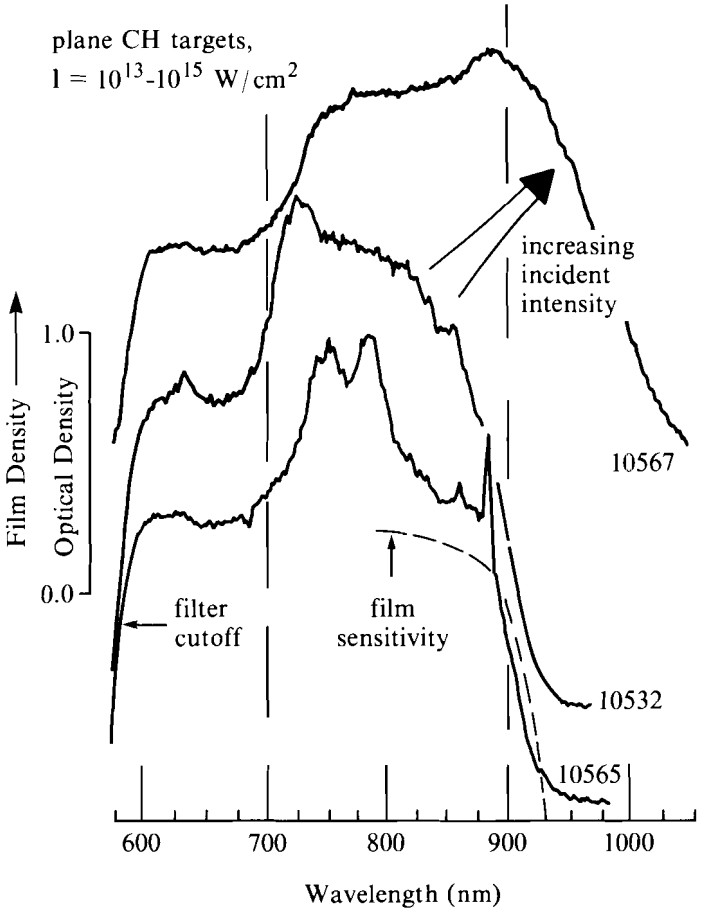

Fig. 34.4
Time-integrated down-scattering spectra arranged in order of increasing incident intensity. The spectral window was limited to $570 < \lambda < 925$ nm by cutoff filters at 570 nm and by the film sensitivity at 925 nm.

The best example of up-scattering, in this geometry, is shown in Fig. 34.5. The three-halves feature around 351 nm dominates the scattering bands and is itself partly blurred by residual 351-nm laser light inadvertently created in the doubling-tripling crystal assembly. In later experiments, the 351-nm laser light was completely suppressed by using the tripling (second) crystal as a doubler and detuning the first crystal. The two up-scattering features are distinctly separated from the three-halves spectrum, one to either side. If we assume that the spectra in Figs. 34.4 and 34.5 are typical and consistent, we can fit them using the enhanced Thomson scattering theory, as shown in Fig. 34.6. Since no x-ray temperature measurement was taken on these shots, we estimate the hot and superhot temperatures to be 7 and 30 keV, respectively. By choosing suitable hot-electron fractions, the observed spectra of two up-scattered peaks straddling the three-halves feature

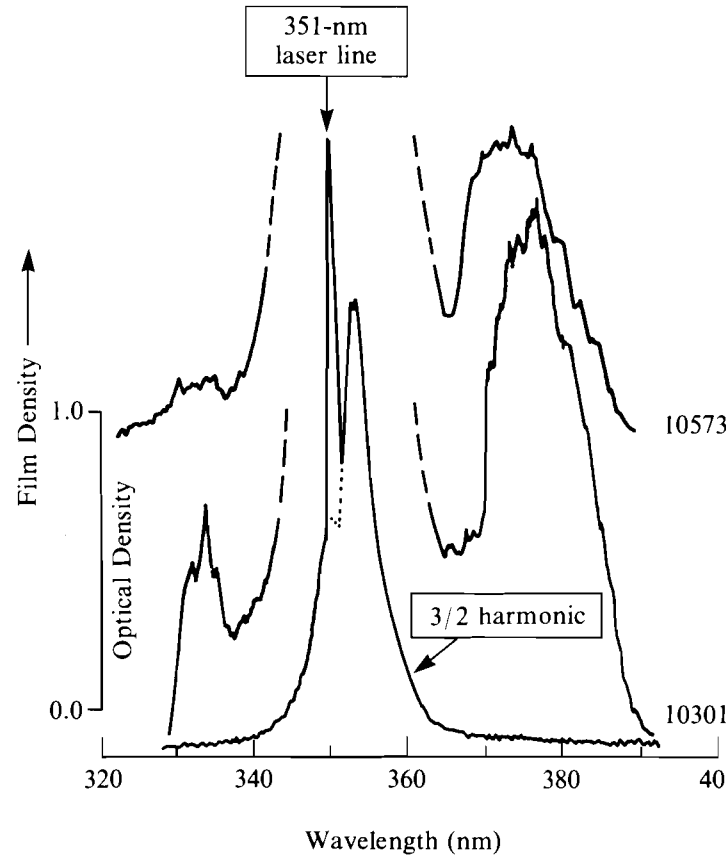

Fig. 34.5
Up-scattering spectra showing the $3\omega_0/2$ signal and two enhanced Thomson scattering features that arise from a hot component of the electron-temperature distribution at 8 to 10 keV and a superhot component at 25 to 30 keV.

and a down-scattered feature near 700 nm can be self-consistently reproduced. The fourth predicted band, above 900 nm, was not observed due to the lack of film sensitivity, except for shot 10567, which was extremely intense and overexposed the film.

Using the same geometry, the down-scattering signal was time resolved, as shown in Fig. 34.7. The time-integrated signal shows the very narrow down-scattering observed at 900 nm and the familiar double-peaked $\omega_0/2$ feature. Due to instrumental restrictions, we have no data below 800 nm for this series of experiments, and no attempt was made to correct the spectra for the frequency response of the detector assembly. The time-resolved picture shows that the $\omega_0/2$ signal turns on well before the ETS signal, as expected if TPD creates the $\omega_0/2$ signal and the superfast electrons that seed the ETS signal. The down-scattering is of very short duration—less than 200 ps—and turns itself on and off at least twice. In most of the experiments using this geometry, the $\omega_0/2$ feature was not observed; in some, however, the down-scattering was evident and had the same temporal history.

We did not consistently observe the half-harmonic signal for three reasons. First, the $\omega_0/2$ emission is strongly peaked in the direction of

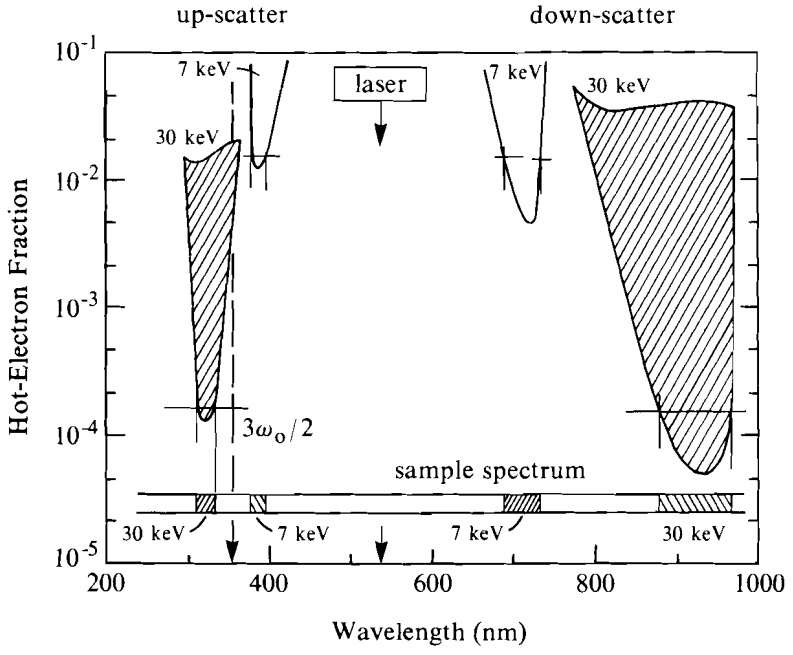

Fig. 34.6
Predicted enhanced Thomson scattering spectral bands for electron-temperature components of 1, 7, and 30 keV. The angle of observation is 45°; the target is normal to the laser and has $Z = 3$. Refraction of the outgoing ETS light is taken into account using a planar plasma blow-off geometry.

the density gradient, which is not the same as the direction of observation. Second, whatever $\omega_0/2$ signal was emitted in the observed direction would be strongly refracted. Finally, since an old S-1 streak tube was used, its sensitivity to 1-μm light was very low.

The experiments using the geometry described by Fig. 34.2(b) were less illuminating. No up-scatter signal was observed at all, primarily because the observations were at 90° from the density gradient. The ETS theory predicts up-scattering signals in this geometry only for $T_{sh} > 60$ keV and then only for extremely large hot-electron fractions (of the order of 10%). The down-scattering data is similar to the following, since the down-scattering geometries were the same.

A series of experiments was conducted using the geometry depicted in Fig. 34.2(c). In this geometry, simultaneous observations were made of the up- and down-scattering in the same direction, along the target normal, which may be assumed to be the direction of the density gradient. We present two down-scattered spectra in Fig. 34.8. On both we can see the large $\omega_0/2$ signal which, because of the choice of target orientation, is not affected by refraction. The position of the down-scattering peak is different for these two shots, even though the average intensities (8×10^{14} W/cm^2) and measured superhot-electron temperatures are the same. We attribute these differences to hot spots in the on-target energy distribution, which varies from shot to shot due to differences in air turbulence in the beamline. We believe that these hot spots are dominating the interaction process described here, especially in terms of the superhot-electron production and

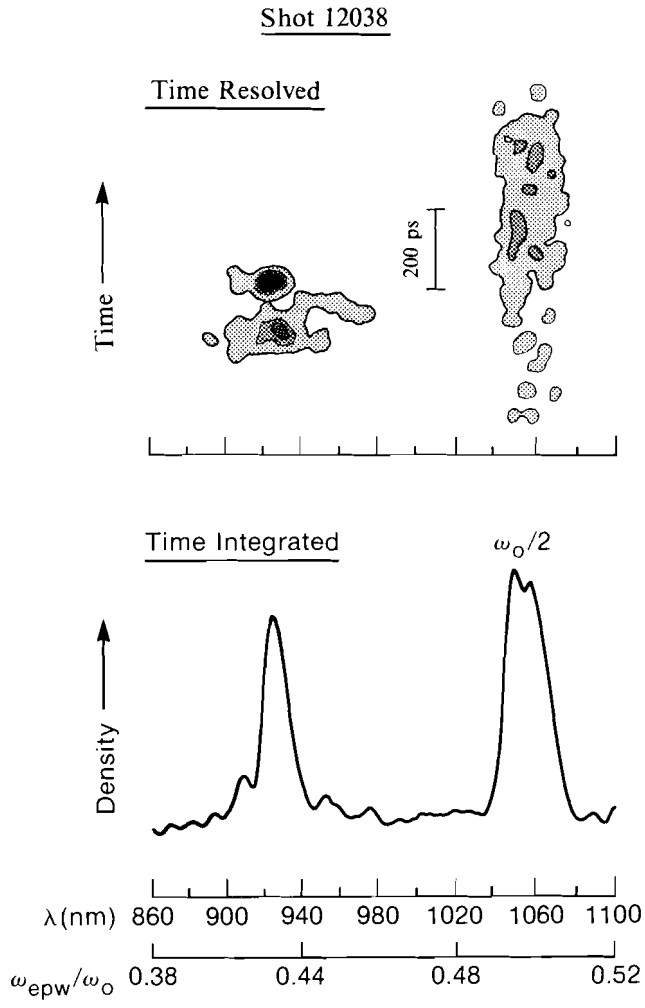

Fig. 34.7
Time-resolved down-scattering spectra. The average intensity was 1 × 10^{15} W/cm^2 in a 1-ns pulse. Note that the $\omega_0/2$ signal turns on before the enhanced Thomson scattering signal.

consequently the enhanced Thomson scattering signal. The absence of the $\omega_0/2$ splitting is attributed to saturation of the streak camera photocathode and the S-1 aging problem already discussed.

The temporal history of this shot, as shown in Fig. 34.9, is similar to Fig. 34.7, showing that the same process is being observed. The ETS signal is of shorter duration (200 ps) than the $\omega_0/2$ signal (700 ps). The half-harmonic signal turns on first and the down-scattering occurs near its peak.

An up-scattering spectrum taken in this same geometry (Fig. 34.10) shows the two peaks associated with ETS. The shorter-wavelength peak, identified with superhot electrons, occurs between $3\omega_0/2$ and $2\omega_0$. The longer-wavelength peak, due to hot electrons, occurs near 400 nm. The latter has been observed regularly, while the former was

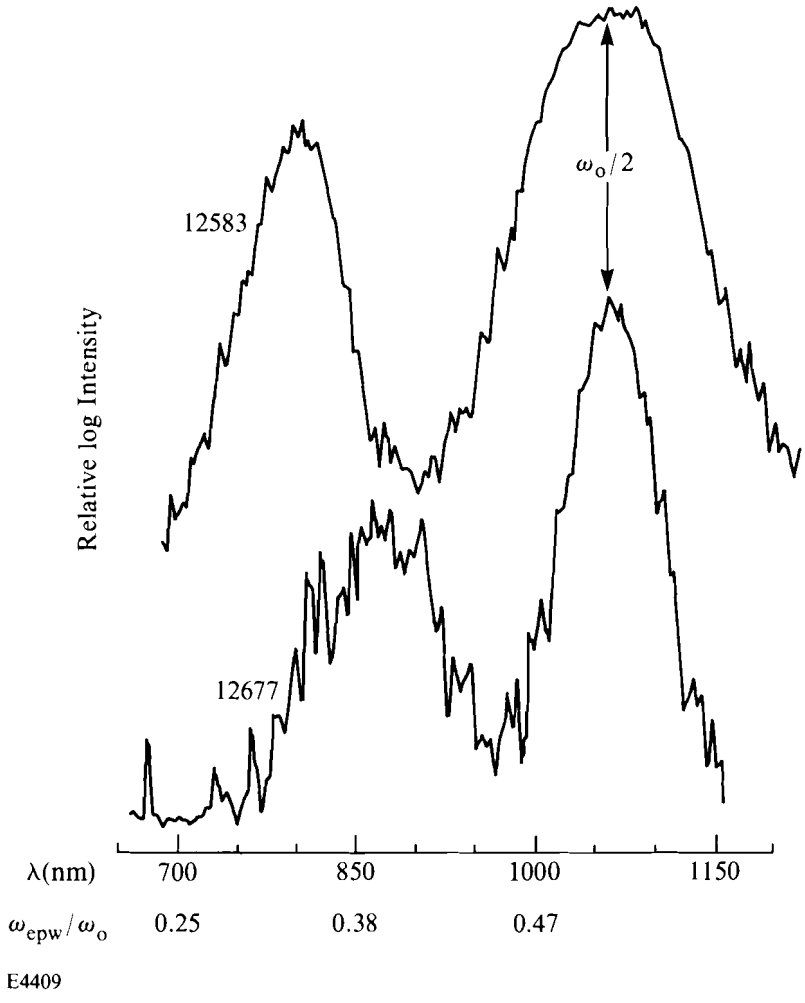

Fig. 34.8
Down-scattered spectra for the same average incident intensity and measured electron temperature. The variations in the position of the bands are attributed to varying hot spots in the incident laser.

visible only rarely. The absence of this peak is presumably due to the lack of enough superfast electrons.

We present a complete description for one particular shot in Fig. 34.11. This shot had a measured average intensity of 7×10^{14} W/cm^2 and a measured superhot-electron temperature of 17 keV. A better theoretical fit was found using a superhot-electron temperature of 30 keV, which is reasonable considering the uncertainties in the temperature diagnostic. A superhot-electron fraction of 1% was found by comparing the measured down-scatter band with Fig. 34.1. This predicts an up-scatter band between 290 and 350 nm, which corresponds well with the measured peak. Since there was no direct measurement of the hot-electron temperature, we assumed a temperature of 17 keV and fit the second up-scatter peak, at a wavelength longer than 351 nm, with a hot-electron fraction of 1%. This value is below the threshold for down-scattering, which is consistent with our observation of only a single down-scattering band

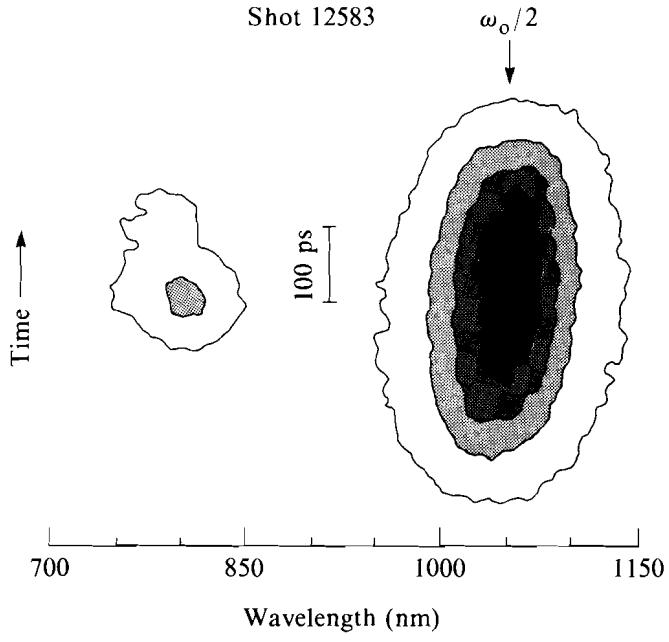

Fig. 34.9
Typical time evolution of the down-scattering spectra, which begins near the peak of the $\omega_0/2$ emission and lasts for about 200 ps.

(from superhot electrons). Therefore, we see that a complete set of data can be explained self-consistently using the ETS theory.

Discussion

The ETS theory describes the results very well for those shots in which a nearly complete set of experimentally measured parameters could be obtained. However, in other instances one or more of the predicted peaks was missing, especially the shorter-wavelength down-scattering band that we have associated with the hot (but not the superhot) electrons. This may be due to the hot-electron fraction not exceeding the threshold needed for enhanced scattering. At other times, the up-scattering band associated with the superhot electrons was also absent, presumably for similar reasons. The lack of sufficient numbers of hot or superhot electrons may be connected to the lack of hot spots in the laser-beam intensity pattern. Since only a limited amount of energy was at our disposal, the up-scattering ETS threshold could only be surpassed in hot spots of the laser beam where the peak intensity could be many times the average intensity. We infer from our measurements that the random distribution of hot spots, presumably due to air turbulence, is responsible for the infrequent appearance of the short-wavelength up-scatter band.

Two other theories could be advanced to explain the existence of the scattered features we observed. The first is convective stimulated Raman scattering (SRS-C).[9] As discussed previously, this interaction takes place in the plasma corona at densities below quarter-critical. According to this theory, the signature is a scattering band that should

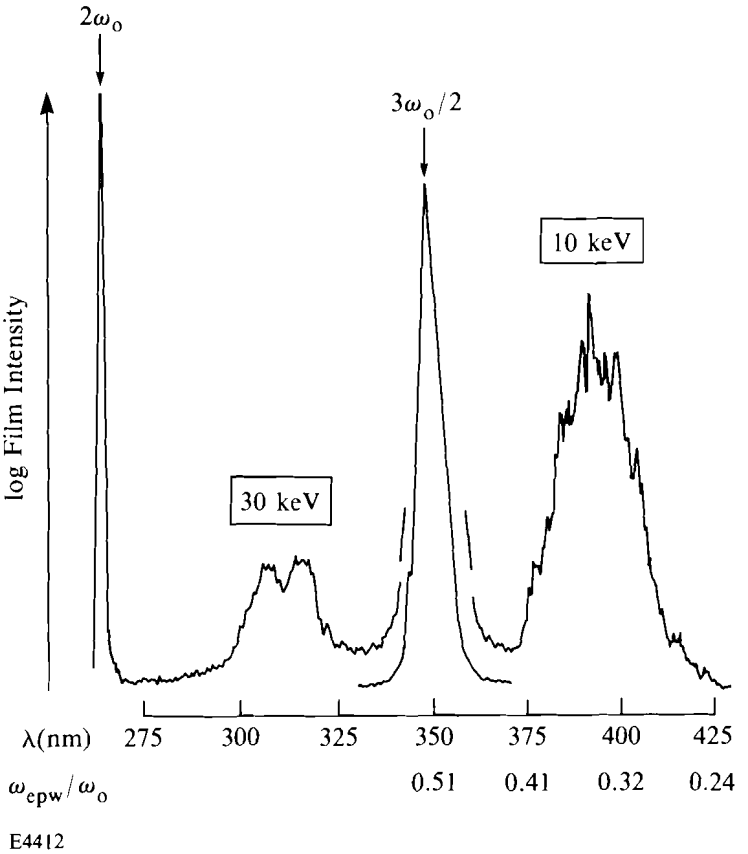

Fig. 34.10
Up-scattering spectrum observed along the density gradient. The two up-scattering features on either side of the $3\omega_0/2$ peak reflect two electron-temperature components with T_h = 10 keV and T_{sh} = 30 keV.

extend from the half-harmonic of the laser up to a higher frequency, where it is cut off by Landau damping (i.e., near $k\lambda_D \approx 0.2$). Density steepening at the quarter-critical surface must be invoked to explain the gap that appears between the down-scattering band and the $\omega_0/2$ feature. In addition, the theoretical threshold for SRS-C is usually not exceeded in the intensity region where down-scattering has been seen.[3] In our experiments, this is certainly the case as well.

Stokes mixing has been suggested as an explanation for the existence of both up- and down-scattering bands[6] because the conditions for the SRS instability also allow coupling to a fourth anti-Stokes EM wave at $w_s' = w_0 + w_{epw}$. Normally, the amplitude of this wave is small, since it is nonresonant. At low plasma densities, and for scattering in the forward direction, the degree of off-resonance is reduced and an appreciable level can be reached. Note, however, that the frequency of this wave lies above the laser frequency by the same amount as the down-scattered wave does below it, and cannot exceed $3\omega_0/2$. Since the dispersion relation for the up-scattered EM wave will not be satisfied at the density where the instability occurs, some propagation of the plasma wave toward a different density will have to be invoked so that the scattered wave will be observable.

Our observations cannot be explained by Stokes mixing since (a) the scattering bands were not symmetric (see Fig. 34.11, where a scale in terms of ω_{epw}/ω_o has been added for convenience), (b) spectral features above the three-halves harmonic were observed (Figs. 34.5 and 34.10) (a region not accessible to Stokes mixing), and (c) our observations in the backscatter direction are incompatible with the resonant condition for up-scattered light since the plasmon wave vector would be too large.

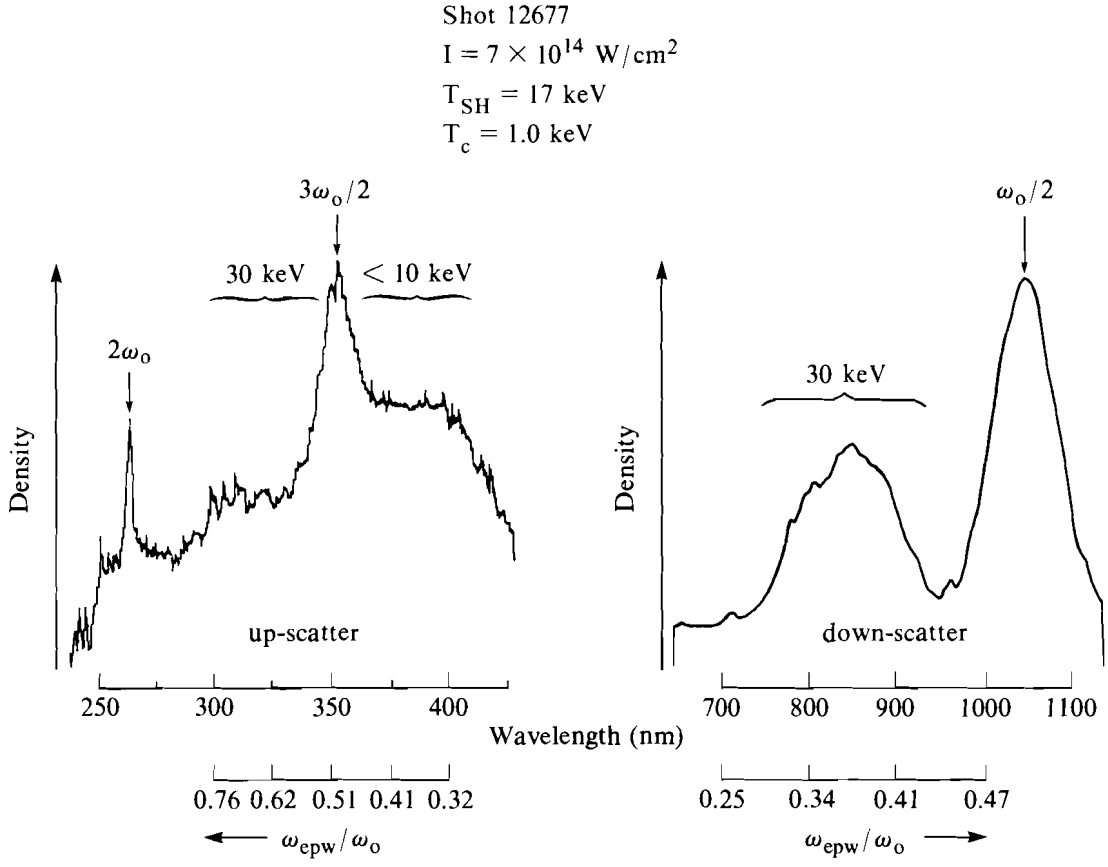

Fig. 34.11
Simultaneous up- and down-scattering spectra. The measured electron temperatures for this shot were T_c = 1.0 and T_{sh} = 17 keV. No hot x-ray component was observed for this shot in the x-ray temperature diagnostic, presumably because of insufficient signal emitted by this component relative to the two other temperature components. The incident intensity was 7 × 10^{14} W/cm^2 in a 600-ps pulse.

In conclusion, we conducted a series of experiments to observe the scattered-light spectrum from a 527-nm laser-produced plasma. We observed three features: one was down-scattered from the laser frequency and two were up-scattered, one on either side of the three-halves feature. Using several different irradiation and observation geometries, we temporally resolved the down-scattered spectra. In addition, we independently measured the continuum x-ray spectra and determined corresponding electron temperatures. We find good agreement with the ETS model if we assume that the electron temperature distribution can be described by three components: a cold background with $T_c \approx 1.5$ keV, a hot component created as a by-

product of resonance absorption or the parametric decay instability with $T_h < 10$ keV, and a superhot component created by the two-plasmon decay instability with $T_{sh} > 15$ keV. We also find that neither convective stimulated Raman scattering nor Stokes mixing is an adequate explanation of the observed spectra.

ACKNOWLEDGMENT

This work was supported by the U. S. Department of Energy Office of Inertial Fusion under agreement No. DE-FC08-85DP40200 and by the Laser Fusion Feasibility Project at the Laboratory for Laser Energetics, which has the following sponsors: Empire State Electric Energy Research Corporation, New York State Energy Research and Development Authority, Ontario Hydro, and the University of Rochester. Such support does not imply endorsement of the content by any of the above parties.

REFERENCES

1. LLE Review **19**, 104 (1984).
2. A. Simon and R. W. Short, *Phys. Rev. Lett.* **53**, 1912 (1984).
3. A. Simon, W. Seka, L. M. Goldman, and R. W. Short, *Phys. Fluids* **29**, 1704 (1986).
4. C. L. Shepard *et al.*, *Phys. Fluids* **29**, 583 (1986).
5. R. E. Turner, D. W. Phillion, E. M. Campbell, and K. G. Estabrook, *Phys. Fluids* **26**, 579 (1983).
6. R. E. Turner *et al.*, *Phys. Rev. Lett.* **57**, 1725 (1986).
7. C. S. Liu and P. K. Kaw, in *Advances in Plasma Physics, Vol. 6*, edited by A. Simon and W. B. Thompson (Wiley, New York, 1976), pp. 83–120.
8. W. Seka, E. A. Williams, R. S. Craxton, L. M. Goldman, R. W. Short, and K. Tanaka, *Phys. Fluids* **27**, 2181 (1984).
9. C. S. Liu, in *Advances in Plasma Physics, Vol. 6*, edited by A. Simon and W. B. Thompson (Wiley, New York, 1976), pp. 121–178.
10. R. S. Craxton (private communication).
11. K. Estabrook, W. L. Kruer, and B. F. Lasinski, *Phys. Rev. Lett.* **45**, 1399 (1980).
12. A. B. Langdon, B. F. Lasinski, and W. L. Kruer, *Phys. Rev. Lett.* **43**, 133 (1979).
13. B. Bezzerides, S. J. Gitomer, and D. W. Forslund, *Phys. Rev. Lett.* **44**, 651 (1980).
14. T. Kessler, W. Seka, J. Kelly, D. Smith, R. Bahr, W. Lockman, N. Wong, and J. Soures, *High Power and Solid State Lasers* (SPIE, Bellingham, WA, 1986), Vol. 622, pp. 156–160.
15. P. A. Jaanimagi (private communication).
16. R. L. Keck, L. M. Goldman, M. C. Richardson, W. Seka, and K. Tanaka, *Phys. Fluids* **27**, 2762 (1984).